International Journal of Plasticity 147 (2021) 103099

Contents lists available at ScienceDirect

International Journal of Plasticity

journal homepage: www.elsevier.com/locate/ijplas

Comparison of full field predictions of crystal plasticity simulations using the Voce and the dislocation density based hardening laws

Chaitali S. Patil [a], Supriyo Chakraborty [a], Stephen R. Niezgoda [a,b,*]

[a] Department of Materials Science and Engineering, The Ohio State University, Columbus, OH, USA
[b] Department of Mechanical and Aerospace Engineering, The Ohio State University, Columbus, OH, USA

ARTICLE INFO

MSC:
00-01
99-00

Keywords:
A. Dislocations
B. Constitutive behavior
B. Crystal plasticity
B. Polycrystalline material

ABSTRACT

Crystal plasticity modeling and simulation is an important predictive tool for understanding the deformation of polycrystalline materials under diverse loading conditions. The validity and accuracy of these simulations depend on the choice of the constitutive law. One of the main components of the constitutive law for plastic deformation is the hardening law. This study, therefore, focuses on understanding the effect of the phenomenological Voce hardening law and the dislocation density based hardening law on full field predictions of crystal plasticity simulations. The crystal plasticity simulations were performed using a three dimensional (3D) fast Fourier transform-based elasto-viscoplastic (EVP-FFT) micromechanical solver for the tensile deformation of copper. Simulation results show that the local distribution of stress strongly depends on the hardening rule. Average texture characteristics predicted by both the laws do not vary significantly. However, spatial orientation evolution (micro-texture) varies with increasing strain. For the Voce law, spatial distribution of the dislocation density calculated from the threshold stress is more homogeneous than the predictions of the dislocation density based hardening law. Finally, our results highlight that a simple dislocation density based storage–recovery model is insufficient to explain the orientation dependence of the stored energy distribution. Hence, careful choice of the hardening law is important for the prediction of localized micromechanical fields.

1. Introduction

Full-field crystal plasticity modeling and simulation is one of the cost-effective tools for understanding evolution of micro-mechanical fields (e.g. stress and strain) during the deformation of polycrystalline materials. In the past, these simulations have been used to analyze evolution of field variables involving a range of loading conditions and physical phenomena such as uniaxial deformation (Slone et al., 2018), cyclic deformation (Cruzado et al., 2018; Eghtesad and Knezevic, 2020), twinning (Paramatmuni and Kanjarla, 2019), static recrystallization (Chen et al., 2015) and dynamic recrystallization (Zhao et al., 2016; Nagra et al., 2020). Crystal plasticity simulations are also implemented to interpret or analyze data from experiments such as the high energy diffraction microscopy (HEDM) (Shen et al., 2020) or the digital image correlation (DIC) (Githens et al., 2020). Additionally, crystal plasticity modeling can be utilized to bridge the length scales between the atomistic and macroscopic continuum simulations for Integrated Computational Materials Engineering (ICME) applications (Panchal et al., 2013). Crystal plasticity simulations are now being increasingly used to generate statistically representative data for the machine learning (Mangal and Holm, 2018) and uncertainty quantification analysis (Ricciardi et al., 2020; Kotha et al., 2020). For any of these aforementioned applications, a

* Corresponding author at: Department of Materials Science and Engineering, The Ohio State University, Columbus, OH, USA.
E-mail address: niezgoda.6@osu.edu (S.R. Niezgoda).

https://doi.org/10.1016/j.ijplas.2021.103099
Received 14 December 2020; Received in revised form 30 July 2021
Available online 5 September 2021

quantitative prediction of local mechanical fields is important; which in turn, depends on the validity and accuracy of the underlying constitutive law used in the crystal plasticity framework.

One of the main aspects of a constitutive law for the plastic deformation is the hardening law used for the evolution of a critical resolved shear stress (CRSS) with increasing deformation. Two commonly used hardening laws for the plastic deformation are the phenomenological Voce hardening law and the dislocation density based hardening law. A variety of characterization techniques have been used to validate either the phenomenological or the dislocation density based constitutive laws. Electron backscatter diffraction (EBSD) and DIC were used to analyze distribution of lattice rotations, strain and slip traces predicted by the phenomenological laws (Buchheit et al., 2005; Rehrl et al., 2012; Lim et al., 2014; Pinna et al., 2015; Guery et al., 2016; Baudoin et al., 2019) or dislocation density based laws (Guan et al., 2017; Zhang et al., 2018). Advanced HEDM characterization of mean orientations (Pokharel et al., 2014), grain average elastic strain (Abdolvand et al., 2018) and spatial distribution of elastic strain (Gustafson et al., 2020) were utilized to analyze predictions of the phenomenological laws. All of these studies observed both similarities and differences between experimental results and model predictions. However, little attention has been given to the effect of hardening law on the field predictions.

Reviews like Roters et al. (2010, 2019) comprehensively discussed the crystal plasticity method and different constitutive laws. However, one to one comparison of the different hardening laws is still not widely available in the literature. Lee et al. (2010) observed that average texture predictions are less sensitive to the variation of the hardening law. On the contrary, Lim et al. (2019) observed that rotations of the single crystals with different initial orientations depend on the choice of the hardening law. However, both of these works did not investigate the effect of the hardening laws on the spatial distribution of orientations or other field variables. Furthermore, Demir and Gutierrez-Urrutia (2020) observed that, in comparison to the phenomenological law, spatial distribution of the strain field predicted by the dislocation density based law was in better agreement with the experimentally observed strain distribution. However, this comparison was carried out at an axial strain of only 1%. Similarly, Sedaghat and Abdolvand (2021) showed that predictions of the dislocation density based hardening laws were in better agreement with experimental observations at 2.7% strain. Such comparisons of simulation results with experiments using the available in situ techniques (DIC, HEDM) are currently limited to a small strain. Hence, simulation studies up to larger strain are necessary to know the similarities and differences between the predictions of the hardening laws. Analysis of field evolution at larger strains is of great practical utility to understand various physical phenomena like recrystallization or damage accumulation and failure of structural materials, which are important for large scale manufacturing processes.

Analytical study of differences in the field predictions with the variation of the hardening laws is greatly difficult; mainly because the evolution of both the kinematic and the internal variables during simulation are interdependent. Initial difference in the hardening behavior will affect predictions of the shear rate, the deformation gradient and the orientation evolution at each material point. This will further lead to variation in the constitutive hardening. Polycrystalline boundary conditions further increase the complexity of the problem. This complexity of the boundary conditions as well as evolving field variables make it imperative to analyze the predictions of the hardening laws numerically. Therefore, we present the numerical analysis of similarities and differences, as well as the issues with two of the most commonly used hardening laws —the Voce hardening and the dislocation density based (DD) hardening laws.

In this study, we focus on the predictions of the texture, effective stress and the dislocation density using these two hardening laws on the same microstructure (nearly uniform) with the same numerical solver, error tolerance and loading conditions. We statistically compare the spatial evolution of these field variables by the two laws. To the authors' best knowledge, such extensive analysis of the spatial evolution of different field predictions of these two laws is not available in the literature. Also, field predictions are compared with available experimental results in the literature.

2. Modeling framework

We employed the fast Fourier transform (FFT) based elasto-viscoplastic formulation (EVP) which was developed by Lebensohn et al. (2012). The FFT based approach was originally proposed by Moulinec and Suquet (1994, 1998) for composite materials. The FFT based algorithm is a computationally efficient framework to solve microstructure based mechanical boundary value problems. This method iteratively finds a converging solution for the stress equilibrium and strain compatibility equations, which also satisfies the constitutive relation at each grid point. The method has been widely adopted (Slone et al., 2018; Paramatmuni and Kanjarla, 2019; Nagra et al., 2020; Berbenni et al., 2020; Marano et al., 2021; Magri et al., 2021) and so will not be reviewed here in detail. Further details of this method and its applications can be found in recent reviews by Roters et al. (2019) and Lebensohn and Rollett (2020).

For an elasto-viscoplastic material, the Cauchy stress tensor ($\sigma(x)$) at material point x during a small-strain increment can be expressed using the Hooke's law as,

$$\sigma(x) = C(x) : \epsilon^e(x) = C(x) : (\epsilon(x) - \epsilon^p(x)) \tag{1}$$

where $C(x)$ is the elastic stiffness tensor. $\epsilon(x)$, $\epsilon^e(x)$ and $\epsilon^p(x)$ are the total, elastic and the plastic strain tensor, respectively. Further, the plastic strain rate, $\dot{\epsilon}^p(x)$ is given by,

$$\dot{\epsilon}^p(x) = \sum_{s=1}^{N} m^s(x)\dot{\gamma}^s(x) \tag{2}$$

Here, N is the total number of possible active slip systems during deformation, while, m^s and $\dot{\gamma}^s$ represent the symmetric part of the Schmid tensor and shear rate on a slip system s, respectively. Schmid tensor is defined as $b^s \otimes n^s$ where b^s and n^s are, respectively, the Burgers and the normal vector for the slip system s. $\dot{\gamma}^s$ is further defined as a function of the resolved shear stress, τ^s, and the state variable(s) of the constitutive relations.In the rest of the text, the explicit spatial dependence of the constitutive equations has been dropped for the east of reading. Commonly, the shear rate on slip system s ($\dot{\gamma}^s$) is given in terms of a power law (Hutchinson, 1976; Asaro and Needleman, 1985) as,

$$\dot{\gamma}^s = \dot{\gamma}_o \left| \frac{\tau^s}{{\tau_c}^s} \right|^n \operatorname{sgn}(\tau^s) \tag{3}$$

where, τ^s is the resolved shear stress (RSS) and ${\tau_c}^s$ is the critically resolved shear stress (CRSS). $\dot{\gamma}_o$ and n are the material parameters representing the reference shear rate and the stress exponent, respectively. The reference shear rate, $\dot{\gamma}_o$, is set equal to the macroscopic strain rate i.e. 0.001/s while the stress exponent, n, is set equal to 20. Higher values of the stress exponent, n, result in numerical instabilities for the Voce hardening law.

2.1. Voce hardening law

The evolution of the critical resolved shear stress (${\tau_c}^s$) is given by ,

$$\dot{{\tau_c}}^s = \frac{d{\tau_c}^s}{d\Gamma} \sum_{s\prime=1}^{N} h^{ss\prime} \dot{\gamma}^{s\prime} \tag{4}$$

where $\Gamma = \sum_{s=1}^{N} |\gamma^s|$ represents the total accumulated shear and $h^{ss\prime}$ takes into account of the self and the latent hardening empirically. $\frac{d{\tau_c}^s}{d\Gamma}$ is calculated using the generalized Voce hardening rule (Tome et al., 1984),

$${\tau_c}^s = {\tau_0}^s + \left({\tau_1}^s + {\theta_1}^s \Gamma\right) \left(1 - \left(\exp \left| \frac{{\theta_0}^s}{{\tau_1}^s} \right| \right)\right) \tag{5}$$

where ${\tau_0}^s, {\theta_0}^s, {\theta_1}^s$ and ${\tau_0}^s + {\tau_1}^s$ are the initial CRSS, initial hardening rate, asymptotic hardening rate and the back extrapolated CRSS, respectively.

2.2. Dislocation density based hardening law

τ_c^s is considered as the internal resistance to dislocation motion due to the short range obstacles like the forest dislocations. Therefore, τ_c^s is given by,

$$\tau_c^s = \tau_0^s + \alpha \mu b^s \sqrt{\sum_{s\prime=1}^{N} \omega^{ss\prime} \rho^{s\prime}} \tag{6}$$

where μ is the shear modulus, b^s is the Burgers vector, τ_0 is initial slip resistance to the deformation and ρ^s is the dislocation density on slip system s. α is a scalar constant for the strength of interactions of the dislocations with a range of geometrical arrangements on different slip systems while $\omega^{ss\prime}$ is the interaction strength parameter. $\omega^{ss\prime}$ represents the probability of dislocation junction formations during the activation of multiple slip systems as well as the collective strength of the resulting junctions (Capolungo, 2011). The average value of the matrix $\sqrt{\alpha^2 \omega^{ss\prime}}$ from both theoretical (Taylor, 1934; Madec et al., 2002) and experimental estimates (Bailey, 1963; Jackson and Basinski, 1967) is approximately within the range of 0.2–0.5. Evolution of statistically stored dislocations (SSD), ρ^s is given by,

$$\dot{\rho}^s = k_1 |\dot{\gamma}^s| \sqrt{\sum_{s\prime=1}^{N} \omega^{ss\prime} \rho^{s\prime}} - k_2 |\dot{\gamma}^s| \rho^s \tag{7}$$

In this equation, the first term on the right-hand side represents the rate of accumulation of the dislocations while the last term represents the rate of annihilation of these dislocations. k_1 and k_2 are the parameters for the rate of the dislocation accumulation and the rate of the dislocation annihilation, respectively. We note here that when only self-hardening is considered, i.e. $\omega^{ss\prime}$ is a diagonal matrix, the equation reduces to the well-known Kocks–Mecking formulation (Mecking and Kocks, 1981; Estrin and Mecking, 1984). Estrin and Mecking (1984), Tomé and Lebensohn (2007) have already established equivalence of the hardening rate of the Kocks–Mecking equation and the Voce hardening rule. However, both the authors assume that the total dislocation density varies with respect to the total shear rate instead of the shear rate on individual slip systems. Moreover, such equivalence cannot be assumed with the incorporation of the latent hardening (in which case, the off-diagonal terms of the hardening matrix are non-zero) in either the Voce or the dislocation density based hardening law.

Here, we considered all coefficients of both $h^{ss\prime}$ and $\omega^{ss\prime}$ equal to unity. It needs to be pointed out that $h^{ss\prime}$ maps the shear increments on slip system $s\prime$ to the effective shear increment on the slip system s (Eq. (5)) for the Voce hardening law, while the $\omega^{ss\prime}$ maps the dislocation density accumulated on the slip system $s\prime$ to the effective dislocation density on the slip system s in the dislocation density based law (Eq. (6)). These two hardening considerations are not equivalent. There is no agreed upon theoretical basis for establishing a one-to-one correlation between the hardening matrix $h^{ss\prime}$ and the interaction matrix $\omega^{ss\prime}$. Use of the isotopic latent hardening will only avoid the additional differences in the field predictions due to the anisotropic latent hardening coefficients. Lastly, we will call the dislocation density based hardening law the 'DD' law and the Voce hardening law as the 'Voce' law in the rest of the text.

Table 1
Model parameters of the Voce hardening law for copper.

Symbol	Description	Value	Unit
τ_0	Initial CRSS	14	MPa
$\tau_0 + \tau_1$	Backextrapolated CRSS	112	MPa
θ_0	Initial hardening rate	260	MPa
θ_1	Asymptotic hardening rate	10	MPa

Table 2
Model parameters of the dislocation density based hardening law for copper.

Symbol	Description	Value	Unit
α_0	Scalar constant for interaction strengths	0.5	–
τ_0^s	Initial slip resistance on slip system s	11.0	MPa
$\rho^{s,initial}$	Initial dislocation density on slip system s	1.0×10^{10}	m^{-2}
k_1	Fitting parameter for the rate of dislocation immobilization	100.0	m
k_2	Fitting parameter for the rate of dislocation recovery	21.0	–

Table 3
Material constants for copper.

Symbol	Description	Value	Unit
b	Burgers vector magnitude	2.56×10^{-10}	m
C_{11}	Elastic constant	169.66	GPa
C_{12}	Elastic constant	122.50	GPa
C_{44}	Elastic constant	75.83	GPa
μ	Shear Modulus	47.50	GPa

3. Results and discussion

A representative volume element (RVE) of the size 128 × 128 × 128 grid points containing 491 grains was constructed using an open-source software Dream.3D (Groeber and Jackson, 2014). In Fig. 1(a), nearly equi-axed grain structure of this RVE is illustrated by its 3D inverse pole figure map, colored according to the tensile axis. In Fig. 1(b), orientation distribution function (ODF) of the same microstructure is plotted in the inverse pole figure. ODF is calculated using De La Vallee Poussin kernel with a half-width of 10°. The maximum intensity for this ODF is slightly greater than one. Hence, we consider the initial texture of the microstructure as approximately uniform. Using this RVE, we calibrated both the models with the experimental tensile test data reported in Bronkhorst et al. (1992). This uniaxial tensile test was performed on the oxygen-free high thermal conductivity (OFHC) copper at room temperature with a strain rate of 0.001/s. Tables 1 and 2 list the calibrated model parameters of the Voce and the DD laws, respectively. Table 3 presents the material constants used for copper. Fig. 1(c) compares the simulated stress–strain curves with the experimental stress–strain curve. The flow stress response of both the models is similar. The inset in Fig. 1(c) presents a magnified portion of the stress–strain curves around true strain of 0.3. We will discuss the variation of field predictions with the Voce and the DD law in the following subsections. Additionally, convergence analysis of the Voce and the DD law is reported in Appendix B while the simulation results with anisotropic latent hardening are reported in the supplementary data.

3.1. Texture

Texture evolution during the tensile deformation of fcc metals results in the formation of a strong ⟨111⟩ fiber and a weaker ⟨001⟩ fiber (Naaman et al., 1987; Stout and O'Rourke, 1989). Both the hardening rules result in this characteristic texture formation. Fig. 2 presents the volume fraction of the ⟨111⟩ and the ⟨001⟩ fibers as a function of the strain. Volume fraction of these fibers were calculated by integration of ODF over a 20° region around the fiber orientation. The angular spread of 20° was chosen to maintain consistency with the available experimental results in the literature (Naaman et al., 1987). We note here that all texture analysis presented in this subsection is carried out by using an open source software Mtex-4.5.2 (Bachmann et al., 2010). There is a slight difference in the volume fraction of both the ⟨111⟩ and ⟨001⟩ fibers between the two hardening laws. The ⟨001⟩ fiber fraction from the DD law is marginally smaller than the prediction of the Voce law. In contrast, the ⟨111⟩ fiber fraction from the DD law is marginally higher than the Voce law. As a result, the ratio of the volume fraction of the ⟨111⟩ fiber to the ⟨001⟩ fiber is slightly higher for the DD law. Evolution of this ratio is further compared with the experimental results (Naaman et al., 1987) in Table 4. The experimental results are reported by Naaman et al. (1987) for tensile test on high purity copper (5N) at the strain rate of 10^{-3}/s. In this experiment, ratio of the volume fraction of the fibers increased from an initial value of 1.45 to 1.70 at 20% deformation. On the other hand, the simulation predictions show an increase from 1.28 to 1.76 for the Voce law and 1.28 to 1.79 for the DD law. Though variations in the ratio due to an initial texture, grain size or deviation from the ideal boundary conditions during an experiment can affect this result, texture evolution from both the hardening laws appears to be faster than the experimental results.

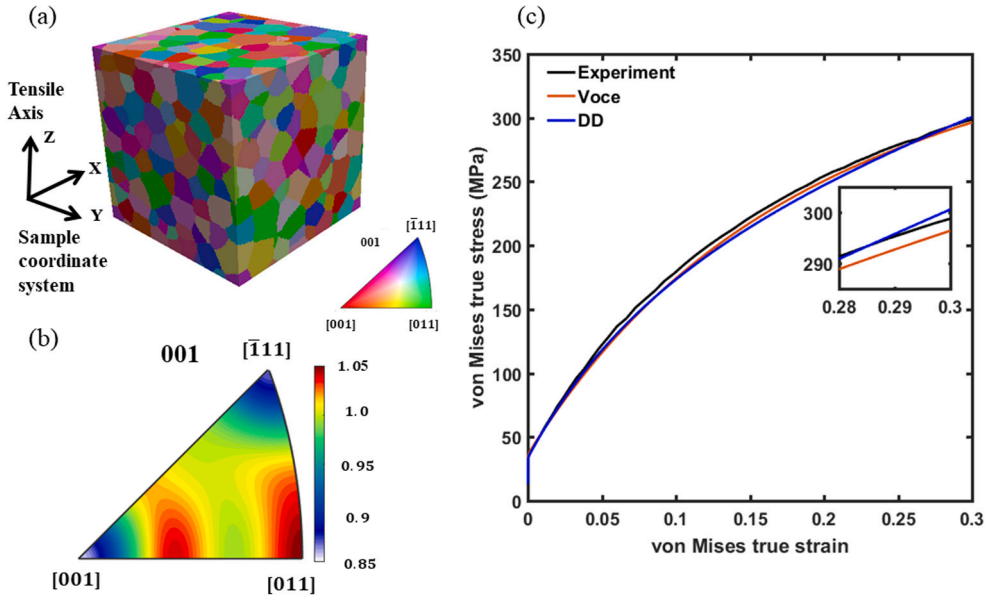

Fig. 1. (a) 3D inverse pole figure map of the initial microstructure colored according to the tensile axis. This RVE containing 491 grains is used for all the simulations. (b) Orientation distribution function (ODF) for the RVE is plotted in the inverse pole figure with respect to the tensile axis. (c) Stress–strain curves predicted by the Voce (red) and the DD (blue) law compared with the experimental uniaxial tensile test results (black) of OFHC copper (Bronkhorst et al., 1992). The inset in this subfigure presents a magnified portion of the stress–strain curves around 30% true strain. For both simulation and experiment, temperature and strain rate were 300 K and 0.001/s, respectively.

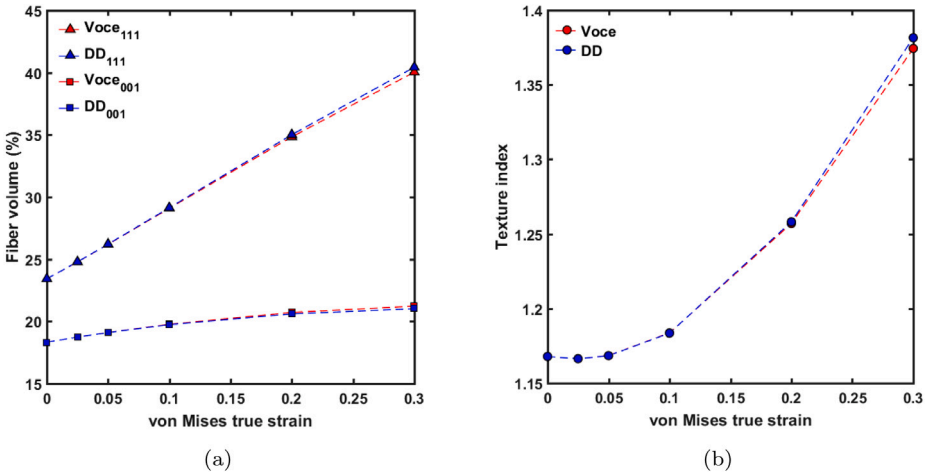

Fig. 2. Evolution of (a) volume fraction of the ⟨111⟩ and the ⟨001⟩ fiber and (b) texture index with von Mises true strain predicted by the Voce and the DD hardening law. Similar trends of the fiber volume fraction and texture index evolution can be observed for both the laws.

Fig. 2 also shows the evolution of the texture index with the strain. Texture index is a scalar parameter to characterize the sharpness of the texture. It is defined as Bunge (2013),

$$J = \oint f(g)^2 \, dg \tag{8}$$

where, g represents orientation and $f(g)$ is the orientation distribution function. In Fig. 2(b), texture index increased from 1.16 to 1.38 for the DD law and from 1.16 to 1.37 for the Voce law after 30% deformation. Thus, it can be concluded from Fig. 2 that the average texture evolution is not significantly changed between the DD and the Voce hardening laws.

To illustrate the differences in the local texture development, Fig. 3 presents the inverse pole figure maps at 5% and 30% strain in the 2D section of the RVE. Fig. 3 also presents a point-to-point difference between the orientations (i.e. disorientation) predicted by the Voce and the DD law. At 5% strain, texture formation is homogeneous across the grains. The disorientation angle is less than 1° for all of the cross sectional area presented in the figure. Instead of any grain specificity, orientation differences can be

Table 4
A comparison of the ratio of volume fractions of the ⟨111⟩ fiber to the ⟨001⟩ fiber.

von Mises true strain	0.0	0.05	0.1	0.2
Experiment (Naaman et al., 1987)	1.45	1.59	1.66	1.70
Voce	1.28	1.37	1.47	1.68
DD	1.28	1.37	1.48	1.70

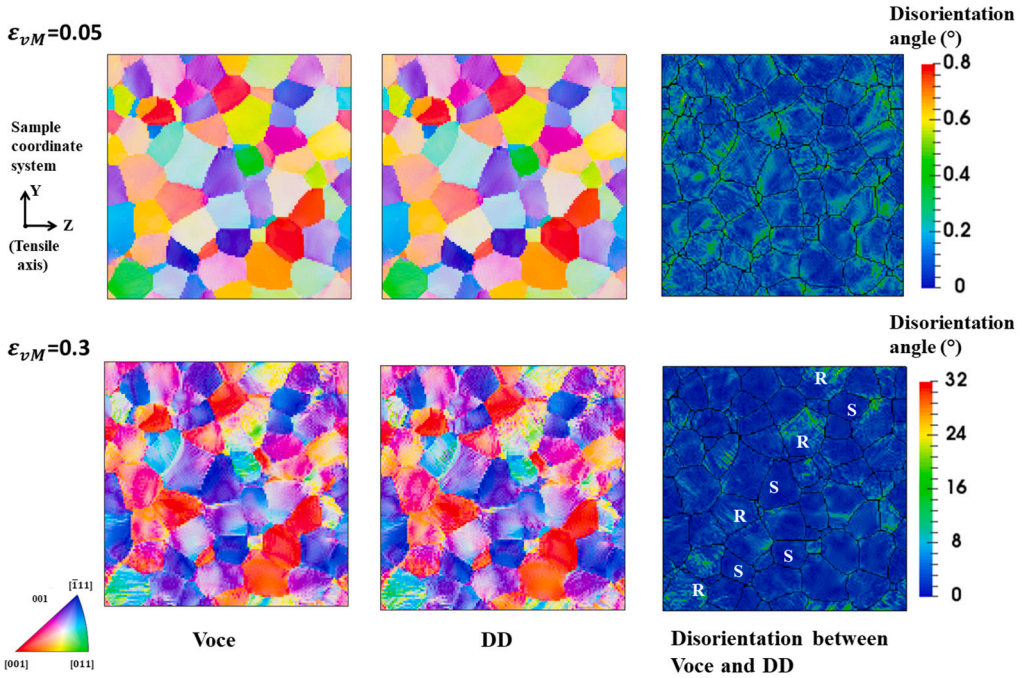

Fig. 3. Inverse pole figure map of the 2D section of the RVE at 5% and 30% strain. Disorientation angles between the local orientation predictions by the Voce law and the DD law are shown in the last column. Few of the grains near ⟨111⟩ orientations which are showing less disorientation angles between the two laws are marked by a letter 'S'. Similarly, grains which are rotating towards either the ⟨001⟩ or ⟨111⟩ orientation and which are showing larger disorientation angles are marked by a letter 'R' .

mainly observed near the grain boundary. The intragranular orientation fields at 30% strain show significant differences between the models. At 30% strain, the deformation texture is more heterogeneous. Intragranular orientation spread can be observed in most of the grains. The disorientation angle between the Voce and the DD law is increased. Although most of the region still shows the disorientation angles less than 5°, few regions show disorientation angles greater than 15°. Visual inspection of the 2D section shows that the grains near the stable ⟨111⟩ orientation, which are marked by the letter 'S' in the disorientation field at 30% strain, show lesser orientation difference between the hardening rules compared to the grain orientations rotating towards the stable ⟨111⟩ or ⟨001⟩ orientations during the deformation. Few of the grains which are rotating towards either ⟨001⟩ or ⟨111⟩ orientations and showing larger disorientations are marked by letter 'R' in Fig. 3.

Fig. 4 presents the statistical summary of the disorientation angles between the local orientations predicted by the Voce and the DD hardening law for the whole RVE. Fig. 4(a) shows the histograms of the disorientation angles at four different true strains. All the distributions are unimodal and skewed towards the low disorientation angles. These distributions become wider with increasing strain. Fig. 4(b) presents the corresponding boxplots for the disorientation angles. The mean and the standard deviation of the disorientation angles are also reported. Even at 30% strain, more than 75% of the material points show less than 5° disorientation angle between the DD and the Voce law. However, the range and the standard deviation of the distributions are increasing with increasing deformation. Therefore, predictions of the spatial orientations by the two hardening laws vary with increasing strain.

Spatial differences in the orientations between the two laws suggest that the prediction of the average misorientation at a point from its neighbors will depend on the choice of the hardening law. These differences will be particularly important for the simulation of recrystallization, where texture of the recrystallized nuclei depends on the details of local texture evolution during the deformation.

Although we observe large disorientation angles, the grain rotation path appear to be similar for both the models. To verify this, we randomly selected 10 grains within 15° of the ⟨111⟩, ⟨001⟩, ⟨112⟩ and the ⟨110⟩ orientations parallel to the tensile axis. The ⟨111⟩ and the ⟨001⟩ are stable orientations while the grains near the ⟨112⟩ and the ⟨110⟩ rotate towards the stable orientations during the

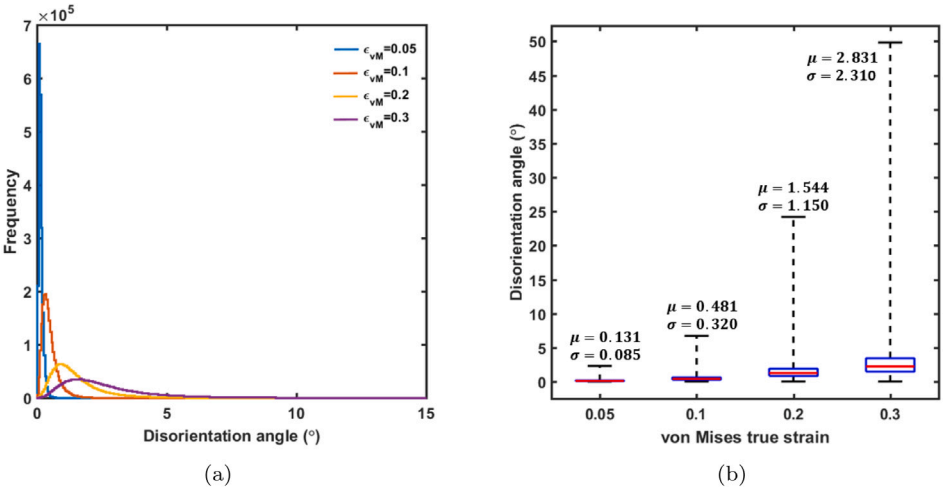

Fig. 4. Statistical summary of the disorientation angles between the orientation predictions of the Voce law and the DD law at 5%, 10%, 20% and 30% true strain is shown using (a) histograms, (b) boxplots. Along with the boxplot, the mean (μ) and the standard deviation (σ) of the disorientation angles are also presented for each strain level.

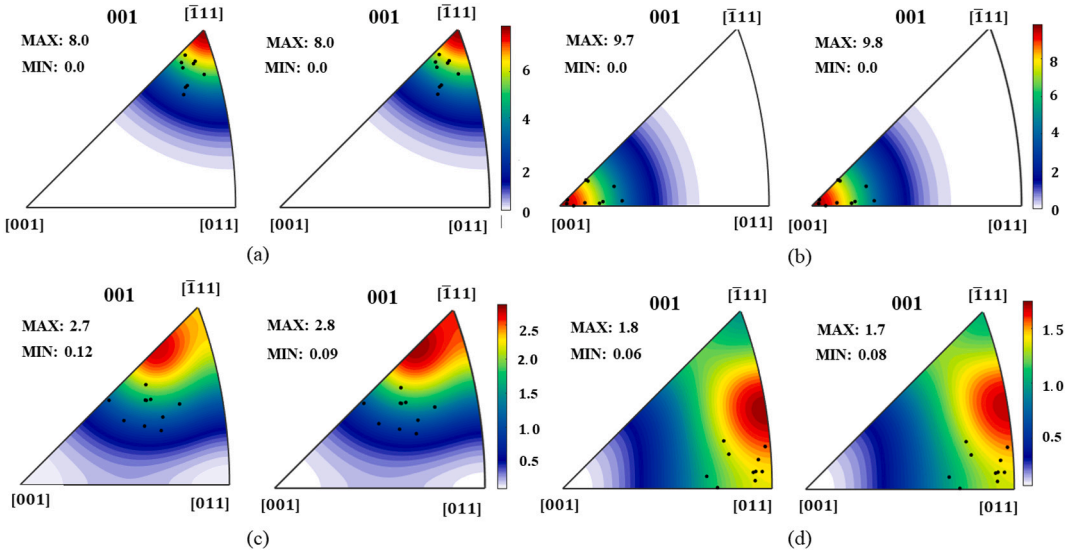

Fig. 5. Inverse pole figures showing the orientation distribution function (ODF) calculated after 30% tensile deformation for 10 randomly selected grains with initial orientation within 15° of the (a) ⟨111⟩, (b) ⟨001⟩, (c) ⟨112⟩, and (d) ⟨011⟩ orientation. Initial orientation of the grains are shown by the black markers in each inverse pole figure. In each subfigure, first inverse pole figure presents the predictions of the Voce law while second inverse pole figure presents the predictions of the DD law.

tensile deformation. Fig. 5 presents the ODFs of these grains plotted in the inverse pole figures at 30% strain. Initial orientations of the grains are shown by the black markers on each of the inverse pole figure. Higher intensities for the grains near the ⟨111⟩ and the ⟨001⟩ orientations suggest lesser orientation spread as against the weaker intensities for the grains near the ⟨112⟩ and the ⟨110⟩ orientations. Magnitude of the minimum and maximum intensities of the ODFs for both the laws are the same for the grains near the ⟨111⟩ orientation. For other three orientations, ODF intensities differ slightly between the two laws. Thus, we observe similarity in the predictions of texture characteristics with small variability in the orientation spread for all four types of the grains.

3.2. Effective stress

We first compare the von Mises true stresses on a 2D section of the RVE at 5% and 30% true strain in Fig. 6. This same 2D section is used for the inverse pole figure map in Fig. 3. The grain boundary network of this 2D section is also overlaid on the stress field for the convenience of visualization. Few of the regions with comparatively higher stress than the average stress of this 2D section (hot

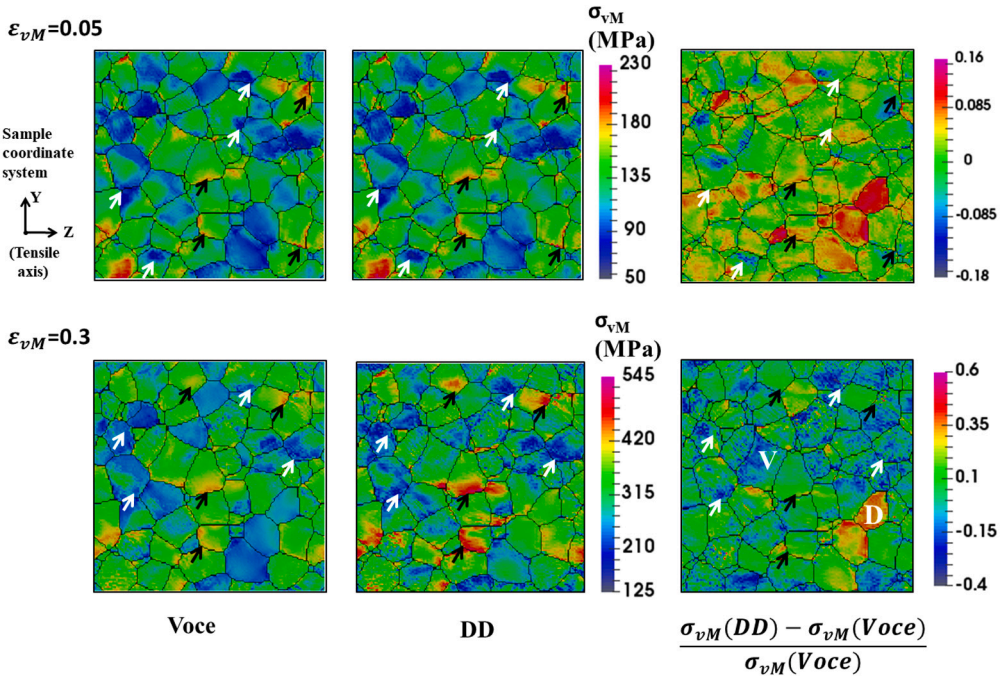

Fig. 6. Distribution of the von Mises true stresses on the 2D section of the RVE predicted by the Voce and the DD hardening laws. Differences between these two stress predictions in terms of fractional change from the prediction of the Voce law at each grid point are shown in the last column. Grain boundaries are delineated by black lines on the stress distributions. Black arrows mark few regions with high stresses (hot spots) while the white arrows mark few regions with low stresses (cold spots). Upper and lower row present the stress distributions at 5% and 30% true strain, respectively. According to the range of stresses at these two strains, two different scaling are used. Both the hot and the cold spots are located at similar positions for the Voce and the DD law. Also, with increasing deformation there is an increase in the stress variations between the two hardening rules. Particularly, local differences in the stresses are significantly larger than the difference between the macroscopic average stresses of the RVE at both the strain levels.

spots) are marked by black arrows. Similarly, few of the regions with comparatively lower stress than the average stress of the 2D section (cold spots) are marked by white arrows. Both of these hot and cold spots can be observed mainly near the grain boundaries. Fig. 6 also shows the fractional change in local stress predictions of the DD law from the Voce law. While a majority of the grains show similar field predictions at 5% strain, few regions show 8%–15% variation in the stress field. With increasing deformation, this variation becomes more prominent. Local differences in the stress distributions can be observed for most of the area of the 2D section at 30% strain. Particularly, 15%–40% variation in the stress can be observed for some of the grains. These local differences in stress fields are considerably higher than the differences in the average stresses of the RVE as observed in Fig. 1(c). Another point to note from this figure is that the locations of hot and cold spot predictions do not differ significantly with the variation of hardening rule.

Fig. 7 presents the statistical summary of the differences in the stress predictions of the whole RVE. Fig. 7(a) shows histograms of the stress differences at four different true strains. All the distributions are unimodal and become wider with increasing strain. Further, Fig. 7(b) presents the quantitative summary of these distributions. In addition to the boxplots, the mean and the standard deviation of the stress differences are also provided. We note three main observations from this figure. First, both the mean as well as the median are within 2% of the local von Mises stress predictions of the Voce law at all four strain levels. Second, even at 30% strain, the first and the third quantiles are within 10% of the von Mises stress predictions of the Voce law. Third, the range and the standard deviation of the distributions are increasing with increasing deformation. As the average response of both the models is calibrated with the same stress–strain curve (Fig. 1), the mean and median values of the differences between the stress predictions are expected to be close to zero. On the other hand, the increasing standard deviation and range denote that the stress predictions vary spatially with increasing strain. Hence, local distribution of the stress predictions is dependent on the choice of the hardening law.

We also observe that the variation in the spatial distribution of the orientations (Fig. 3) is different from that of the effective stress (Fig. 6). To understand this difference, Fig. 8 presents the distribution of the CRSS and the ratio of the resolved shear stress to critical resolved shear stress (X) on the most active slip system of a grain at 30% strain. It is apparent from the figure that the spatial variation in τ/τ_c is not necessarily equivalent to spatial variation of the τ_c. In Eq. (3), the reference shear rate ($\dot{\gamma}_0$) and stress exponent (n) are the same for both the Voce and the DD laws. Hence, spatially different evolution of the critical resolved shear stress (τ_c) on individual slip system can result in different evolution of the τ. This different evolution of τ will result in different von Mises true stresses. On the other hand, we note from Eq. (3) that τ/τ_c on an individual slip system influences the shear rate ($\dot{\gamma}$), which in turn influences the plastic spin ($\dot{\omega}_p$) (Eq. (A.1)). As the evolution of the $\dot{\omega}_p$ determines the texture evolution, the texture

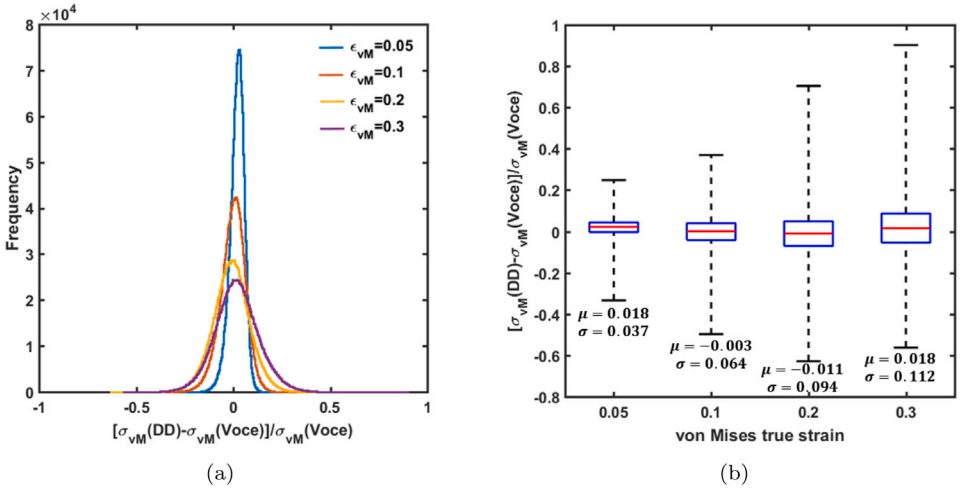

Fig. 7. Statistical summary of the differences in the von Mises true stress predictions by the Voce law and the DD law at 5%, 10%, 20% and 30% true strain is shown using (a) histograms and (b) boxplots. Along with the boxplot, the mean (μ) and standard deviations (σ) of the stress differences are also presented for each strain level. Stress differences are normalized by von Mises true stresses of the Voce law.

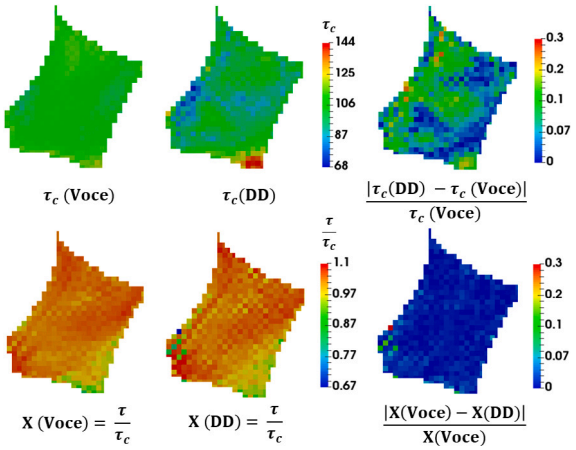

Fig. 8. Distribution of the CRSS (τ_c) and the ratio of the resolved shear stress to critical resolved shear stress (X=τ/τ_c) on the most active slip system of a grain at 30% strain predicted by the Voce and the DD hardening laws. Differences between these predictions in terms of fractional change from the prediction of the Voce law at each grid point are shown in the last column.

evolution is mainly governed by the τ/τ_c. Therefore, as the spatial variations of the τ_c and τ/τ_c are different, spatial distributions of the stress and textures are different between the two laws.

3.2.1. *Grain orientation and grain size dependence of the effective stress*

In Fig. 6, few grains like the one marked by a letter 'D' show higher stresses by the DD hardening while few grains like the one marked by a letter 'V' show higher stresses by the Voce hardening. In order to understand the grain specificity of such stress differences, we present the grain size and orientation dependence of the stress predictions of the Voce and the DD law in Fig. 9. Fig. 9(a) and 9(b) illustrate orientation dependence of the grain average stresses. The Taylor factor is used as a parameter to describe the initial orientations of the grains. Stress prediction by the DD law show more scatter for all the orientations than predictions of the Voce law. The Voce law particularly predicts lower stresses for the grains with low Taylor factor than the grains with the higher Taylor factor. Orientation dependence of the stress differences between the DD and the Voce law is apparent from Fig. 9(b). Predictions of the DD law are more than 15% higher than the predictions of the Voce law for the grains with Taylor factor lower than 2.5. This region is marked by a black box in Fig. 9(b). For other orientations, stress difference is smaller and spread nearly equally in the positive and negative range, i.e. stress variation is less specific for these grains.

Additionally, Fig. 9(c) shows the average von Mises true stress of the grain ($\langle\sigma_{vM}\rangle$) as a function of the equivalent spherical diameter of the grain ($\langle$ESD$\rangle$). Average grain stress is normalized by the mean stress of the RVE ($\overline{\sigma}_{vM}$) while $\langle$ESD$\rangle$ of the grain is normalized by the mean grain size of the RVE ($\overline{\text{ESD}}$). Most of the grains have average grain diameter between 0.5–2.0 times the

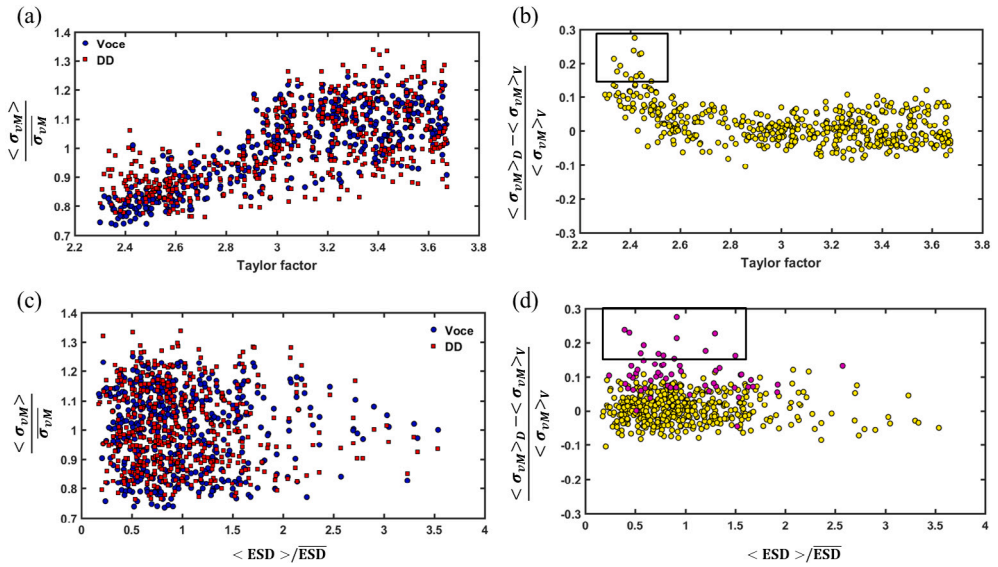

Fig. 9. (a) Normalized grain average stresses as a function of the Taylor factor. Average grain stress is normalized by the mean stress of the RVE ($\overline{\sigma}_{vM}$). (b) Fractional changes of grain average stresses from predictions of the Voce law as a function of the Taylor factor. The region where difference between the stress predictions is higher than 15% is marked by a black-box. (c) Average von Mises true stress of the grain ($\langle\sigma_{vM}\rangle$) as a function of the equivalent spherical diameter of the grain ($\langle$ESD$\rangle$). $\langle$ESD$\rangle$ of the grain is normalized by the mean grain size of the RVE ($\overline{\text{ESD}}$). (d) Fractional changes of grain average stresses from predictions of the Voce law as a function of the normalized $\langle$ESD$\rangle$ of a grain. Grains with Taylor factor less than 2.5 are specifically marked by a magenta color. The region where difference between the stress predictions is higher than 15% is marked by a black box.

mean diameter of the RVE. In this range, both the DD as well as the Voce hardening law show a large scatter in the stress predictions with no specific grain size dependence. Although, the number of grains larger than twice the average diameter is relatively smaller, for these grains, the von Mises stresses by both the laws tend to approach the mean stress of the RVE. Fig. 9(d) further presents the fractional change of the grain average stresses predicted by the DD law from the grain average stress predictions of the Voce law as a function of normalized grain size. For most of the grains, stress differences are smaller than 15%. However, some of grains with normalized grain diameter within 0.5 to 1.5 show larger stress differences as marked by the black box in Fig. 9(d). As we observed that the grains with Taylor factor less than 2.5 show larger difference in the stress predictions, these grains are specifically colored with different color (Magenta) in the figure. Almost all of the grains in the highlighted black box have Taylor factor less than 2.5. Thus, the differences in the stress predictions are less specific with respect to the grain size but depend strongly on the initial orientations of the grains. We note that the grains within 20° of the $\langle 001 \rangle$ orientation have Taylor factor less than 2.5. As we observe significant stress variations for these grains, we will conduct more analyses of these grains in a later section.

From the results presented in this subsection we can conclude that the stress distributions vary spatially with variation of the hardening law. Therefore, careful choice of the hardening law is important to understand the plastic deformation at the grain scale and below. For example, effective stress is commonly used as a failure metric to predict damage nucleation (Naragani et al., 2017). Thus, the spatial variation of stress distribution will have an effect on the prediction of damage nucleation and propagation. Also, Kanjarla et al. (2012) have shown that intra-grain stress heterogeneity (Type II) has a greater influence than the mean average stresses (Type I) in diffraction peak broadening. As the comparison of experimental results and constitutive model predictions is becoming an important tool for data analysis of HEDM experiments, our results emphasize the need for detailed experimental studies with the aim of validating specific constitutive laws to provide confidence in such analysis.

3.3. Dislocation density

Fig. 10 presents the accumulated shear strain, CRSS and dislocation density for one of the active and inactive slip systems of a single grain at 30% strain. From Fig. 10(a), we observe that the total shear accumulated on the active slip system is significantly higher than the total shear accumulated on the inactive slip system. Moreover, in Fig. 10(b), CRSS is similar on both of the slip systems for the Voce as well as the DD law. Fig. 10(c) presents the dislocation density predictions from both the laws. For the Voce law, the dislocation density is back-calculated from the CRSS using the Taylor equation,

$$\rho_s = \left(\frac{{\tau_c}^s}{\alpha \mu b} \right)^2 \tag{9}$$

here, μ and b are the shear modulus and the Burgers vector, respectively. α is a material constant which takes into account average strength of the dislocation interactions. Consistent with Eq. (6) for dislocation density based law, value of α is set equal to 0.5.

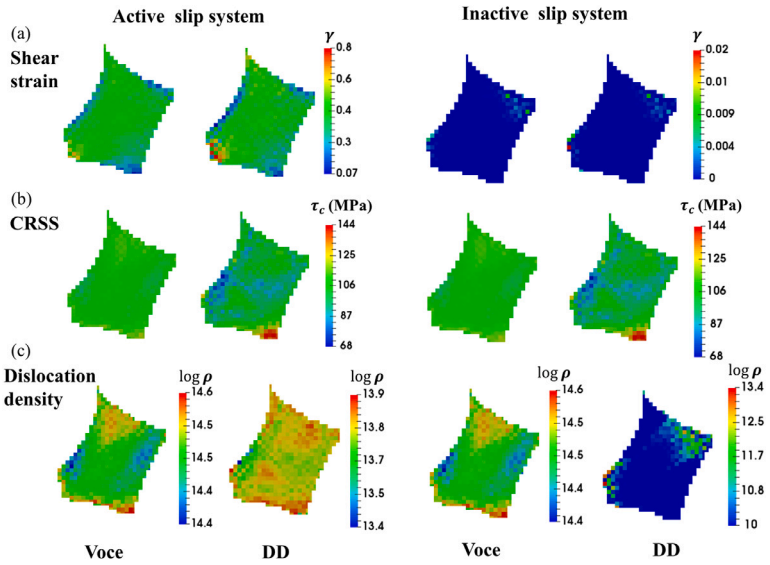

Fig. 10. Distribution of the total shear strain, CRSS and dislocation density for an active and inactive slip system on the 2D section of a grain at 30% strain predicted by the Voce and the DD hardening laws.

In case of the Voce law, similar to the CRSS evolution, dislocation density accumulation is also similar on active and inactive slip system (Fig. 10(c)). Given the isotropic latent hardening used in both the laws, similar evolution of CRSS on different slip systems is understandable. Consideration of the latent hardening assumes that dislocation accumulation on intersecting slip planes also affects the CRSS on individual slip system. Hence, the CRSS is representative of the collective resistance from dislocations on the intersecting slip planes as well as resistance from the in-plane dislocations. Therefore, CRSS will evolve for both active and inactive slip systems. Also, as the CRSS represents the average resistance of the dislocations, dislocation density back-calculated from the CRSS is also representative of the dislocations on the intersecting and in-plane dislocations instead of the dislocations on the individual planes. On the other hand, dislocation density is the internal variable in the DD law. In this case, evolution of the dislocation density is affected by the shear rate on the individual slip system (see Eq. (7)) and evolution of the dislocation density on the active slip systems is different than the evolution of dislocation density on the inactive slip system. Hence, the DD law can predict the dislocation density distributed on the individual slip planes, while, it is difficult to correlate the dislocation densities on the individual planes with CRSS using the Voce law. Further, we note that summation of the dislocation densities for all slip systems as Adam et al. (2018),

$$\rho_{total} = \sum_{s=1}^{N} \left(\frac{{\tau_c}^s}{\alpha \mu b} \right)^2 \tag{10}$$

will result in the overestimation of the dislocation densities, as the dislocation densities will be counted more than once for different slip systems. Instead, better alternative to predict the dislocation density is calculating the average CRSS from the all slip systems $\left(\frac{\sum_{s=1}^{N} \tau_c}{N} \right)$ and use this average CRSS for the dislocation density predictions as Kim et al. (2017),

$$\rho_{total} = \left(\frac{\sum_{s=1}^{N} {\tau_c}^s}{\alpha \mu b N} \right)^2 \tag{11}$$

Using Eq. (11), the mean dislocation density of the RVE calculated from the Voce law is $3.07 \times 10^{14} \mathrm{m}^{-2}$ while the mean dislocation density estimated by the DD law is $2.58 \times 10^{14} \mathrm{m}^{-2}$ at 30% true strain. For polycrystalline copper, Bailey (1963) reported mean dislocation density of $5.70 \times 10^{14} \mathrm{m}^{-2}$ after 30% tensile deformation, while, Jiang et al. (2015) reported mean geometrical necessary dislocation density of $5.30 \times 10^{14} \mathrm{m}^{-2}$ after 40% tensile deformation. Thus, in comparison to the experimental observations, both the laws slightly under-predict the mean dislocation density.

In Fig. 11, we present the spatial distribution of dislocation density at 30% strain predicted by both the hardening laws on the 2D section of the RVE. This same 2D section is used in Figs. 3 and 6. In Fig. 11, black arrows point out few high dislocation density regions, while, white arrows show few low dislocation density regions. Fig. 11 also presents the dislocation density normalized by the mean dislocation density of the RVE ($\bar{\rho}$). The distribution of dislocation density predicted by the DD law is more heterogeneous compared to the Voce law. Qualitatively, the Voce law also predict low and high dislocation density regions similar to that of the DD law, as marked in Fig. 11 by the white and black arrows, respectively. However, both hot and cold spots are more localized for the DD law than for the Voce law.

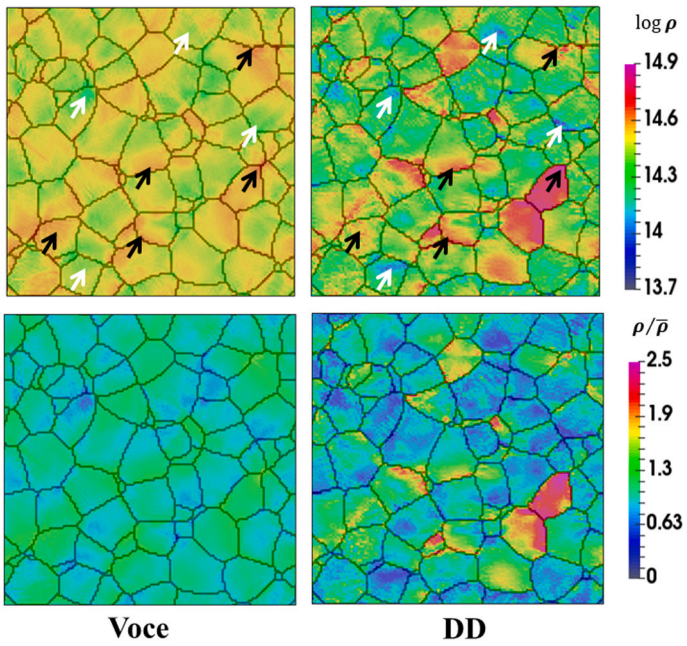

Fig. 11. Upper row presents the distribution of the total dislocation density at 30% strain on the 2D section of the RVE predicted by the Voce (Eq. (11)) and the DD hardening laws. Grain boundaries are delineated by black lines on the dislocation density distributions. Black arrows mark few of the regions with high dislocation density while white arrows mark few of the regions with low dislocation density. Bottom row presents the distribution of total dislocation density normalized by the mean dislocation density of the RVE ($\bar{\rho}$).

Stored energy (proportional to dislocation density) is used to predict the nucleation and growth of a recrystallized nuclei during the recrystallization simulations (Chen et al., 2015; Zhao et al., 2016) or to provide energy based criterion for the crack nucleation predictions (Wan et al., 2014). Larger homogeneity of the dislocation density in the Voce law can have adverse effects during recrystallization or crack propagation simulations.

3.4. Grains near the ⟨001⟩ orientation

We observed in Fig. 9(d) that stress predictions differ between the Voce and the DD law for the grains with Taylor factor less than 2.5 (which are the near ⟨001⟩ ||tensile axis grains). For understanding the hardening behavior of these grains, Fig. 12 presents the average shear stress–strain behavior of two different grains within 15° of the ⟨001⟩ orientation. The average resolved shear stresses for only two of the most active slip systems are presented in the figure. The grain considered in Fig. 12(a), called G1, can be observed in Fig. 6 marked with a letter 'D' to denote a higher stress prediction by the DD law. For this grain, average shear strain predicted by the DD law is lower than the Voce law for both of the slip systems in consideration. Up to 5% strain, difference in the shear accumulations is relatively small. However, difference in the shear accumulation increases with increasing deformation, as the slip systems harden more for the DD law than the Voce law. At 30% strain, the average shear stress predicted by the DD law is approximately 30 MPa higher than the Voce law on both of the considered slip systems. For the grain presented in Fig. 12(b), called G2, the shear strain predictions are nearly equivalent while the shear stresses differs between 20–30 MPa for the two laws at 30% strain. Thus, evolution of CRSS in the ⟨001⟩ grains for the Voce law differs from the predictions of DD law. For these grains, the Voce law show earlier saturation of the CRSS than the DD law.

The higher hardening rate of the ⟨001⟩ grains can be attributed to the higher accumulation of dislocation density during the deformation. Higher the dislocation density, higher the CRSS, resulting in higher hardening rate during the deformation. Therefore, Fig. 13 presents the average dislocation density for each grain ($\langle\rho\rangle$) as a function of the Taylor factor. Average dislocation density of the grain is normalized by the average of dislocation density of the RVE ($\bar{\rho}$). Fig. 13 also presents the orientation dependence of the dislocation density back-calculated from the Voce law for the purpose of completeness. The dislocation density predictions show larger scatter for the DD law than the Voce law. In the case of the DD law, grains with lower Taylor factor show higher dislocation accumulation than mean dislocation density of the RVE. Higher accumulation of dislocations can be either due to the higher dislocation storage or the lesser dynamic recovery during deformation.

Multiple slip systems activate within the grains near the ⟨001⟩ orientation. It is thus expected that the accumulation of the dislocations from all different slip systems will result in the higher hardening of these grains during early stages of the deformation. Vorbrugg et al. (1971) and Takeuchi (1975) observed such higher hardening of the ⟨001⟩ single crystals than other crystal orientations. However, the hardening rate for the ⟨001⟩ crystals decreased significantly with increasing deformation in both

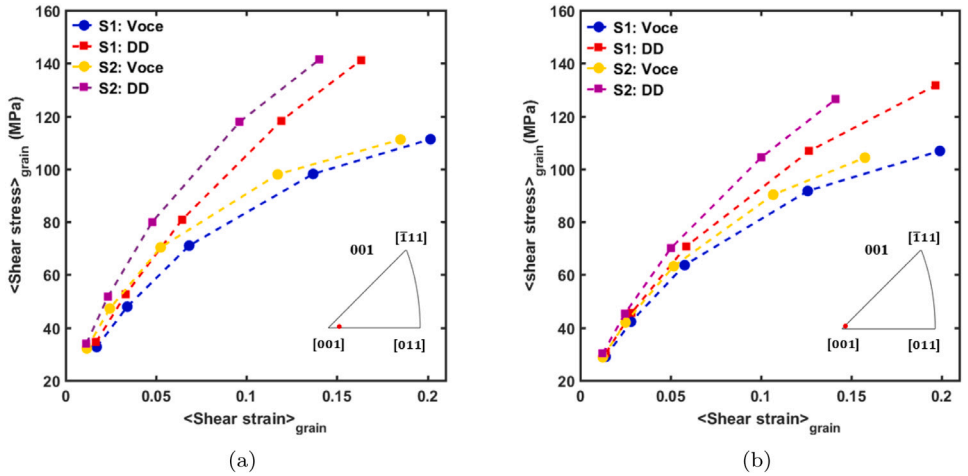

Fig. 12. Evolution of average shear stress as the function of average shear strain for the two slip systems with the highest slip activity (S1 and S2) in grains (a) G1, (b) G2. Initial orientation of both of these grains is marked in the inverse pole figure by a red marker. Predictions of both the Voce and the DD law are shown.

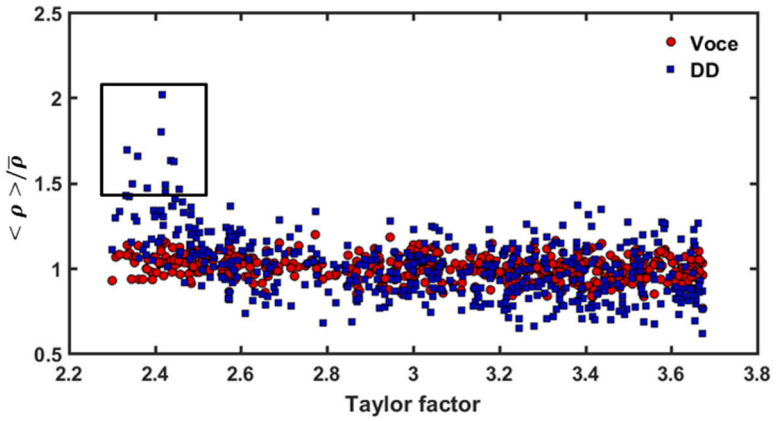

Fig. 13. Normalized average dislocation density in all the grains of the RVE versus the Taylor factor. Predictions of both the Voce and the DD law are shown.

of the experiments. This decrease in the hardening rate can be attributed to the dynamic recovery of the ⟨001⟩ crystals during the tensile deformation. Though it is not expected that ⟨001⟩ grains in polycrystals will follow the exact hardening behavior as in the single crystal experiments, recovery mechanism observed in the single crystals is expected to operate in the polycrystals as well. Moreover, X-ray peak broadening characterization by Sam and Adams (1986) revealed that the stored energy of the grains with the ⟨111⟩ component is nearly 5 times that of the grains with the ⟨001⟩ component after 37% tensile deformation. In terms of the geometrically necessary dislocations also, it has been observed that grains with the ⟨111⟩ orientations have higher dislocation density than the grains with the ⟨001⟩ orientation during tensile deformation of polycrystalline copper (Jiang et al., 2015). Hence, we conclude that the functional form of the inplane recovery (Eq. (7)) with the isotropic latent hardening considered in the current DD model is not sufficient to capture the orientation dependence of the recovery for the grains near the ⟨001⟩ orientation. We also note that this form of the dislocation recovery is commonly used within the DD models (Mecking and Kocks, 1981; Ma and Roters, 2004; Lim et al., 2014). Additionally, models consider recovery due to the dislocation climb. However, formation of the point defects and resulting climb controlled recovery during the deformation should be negligible at the considered deformation strain intervals (0–0.3) and temperature (300 K).

Two potentially necessary model modifications which should be included in the DD models for more realistic distribution of dislocations are the incorporation of the anisotropic latent hardening and the consideration of additional mechanisms of dynamic recovery, such as cross slip of the dislocations. Use of anisotropic latent hardening with smaller interaction coefficients for the slip system pairs which activate within the ⟨001⟩ grains will change the distribution of the dislocations for these grains. Discrete dislocation dynamics (DDD) simulations recommend different values of interaction strengths with large interaction anisotropy (Madec and Kubin, 2017; Sills et al., 2018). However, very large anisotropy suggested by the DDD models can further affect the texture evolution. Also, experimentally it is observed that the effect of initial anisotropy decreases significantly with

increasing deformation (Franciosi, 1985). Additionally, in case of the small anisotropy for the DD model, higher accumulation of the dislocations for the grains with low Taylor factor still persists (Supplementary Fig. 5). Hence, additional experimental and simulation study is required to delineate the effects of anisotropy in dislocation interaction on the distribution of stored energy and texture development during the deformation.

In the case of the dynamic recovery, cross slip of screw dislocations can play an important role for the grains near the ⟨001⟩ orientation. These grains show elongated cell structure in both the single (Mughrabi et al., 1986) as well as polycrystalline copper (Huang, 1998). Cross slip is considered as the necessary precursor for the formation of such dislocation structure (Jackson, 1983). Moreover, Bonneville et al. (1988) explained the orientation dependence of the recovery during the tensile and compression tests of pure copper based on the ease of cross slip of dislocations for different orientations. Similarly, Kubin et al. (2009) emphasized the importance of the orientation dependent dynamic recovery for the fcc materials. Although very few crystal plasticity models e.g. Alankar et al. (2012), Demir and Gutierrez-Urrutia (2020) do consider the recovery based on the cross slip mechanisms, the effect of the cross slip on the orientation and stored energy distribution in crystal plasticity simulations is yet to be studied. Also, very recently a number of independent studies have shown both the Schmid and the Escaig stresses (on the glide and the cross slip planes) influence the activation barrier for the cross slip of dislocations in fcc materials (Esteban-Manzanares et al., 2020; Kuykendall et al., 2020; Malka-Markovitz et al., 2021). Crystal plasticity models which incorporate influence of these stresses on the cross slip, and in turn orientation dependence of the dynamic recovery, need to be developed and validated, specifically for the grains near the ⟨001⟩ orientations. Hence, even though the Voce law predicted lower stress and lower dislocation density in the ⟨001⟩ grains, the DD law has more potential to predict realistic hardening and softening transition in the ⟨001⟩ grains when relevant physics is incorporated.

3.5. Outlook and additional remarks

We note here that the fitting parameters of both the DD law and the Voce law are not unique. However, strain hardening rates cannot be calibrated with large variation of the material parameters as the arbitrary variation in the parameters will change the work hardening behavior. Hence, the possible variation in the parameter space for both the laws is greatly limited for the given calibration curve (e.g. experimental stress–strain curve). Having said this, we agree that the magnitude of the parameters will depend on the considered physical variables, e.g. the hardening matrices. These variations of the parameters will then also affect the magnitude of the field predictions. However, the comparative differences in the different model predictions will still persist. We have shown the results with different set of the fitting parameters for both the Voce and the DD law in the supplementary data. Further, we maintained the power law form in both the DD and the Voce law to maintain consistency in the form of constitutive model. In the case of the DD law, the exponential equation for the velocity predictions and the Orowan's equation for the shear rate predictions are more commonly used. These changes can further influence the field predictions. Also, both of the laws considered in the present study do not explicitly consider the effect of length scale on the flow stress evolution. Many strain gradient based crystal plasticity models are being continuously developed (Wulfinghoff and Böhlke, 2015; Haouala et al., 2020). Effect of incorporation of the length scale as well the magnitude of the length scale should be independently analyzed. Similarly, complexity of grain boundary interactions with dislocations and slip transmissions (Albiez et al., 2019; Linne et al., 2020) as well as their effect on the evolution of the field variables can be studied in the future. Finally, our results highlight the necessity of careful experimental validations of local mechanical fields at larger strains.

4. Conclusions

In this work, we presented a detailed comparison of the phenomenological Voce hardening law with the dislocation density based hardening law (DD law). We quantitatively studied the variation in the average as well as the spatial distribution of the effective stress, orientations and the dislocation density between the two laws and compared the simulation results with available experimental data. Our results emphasize that careful choice of a hardening law is important to understand the plastic deformation at the grain scale and below. Following are the main conclusions from this study:

1. At small strain of 5%, significant variation in the spatial distribution of the orientations is not observed. Also, the average texture development is similar for the Voce and the DD law up to 30% strain. With isotropic latent hardening, texture development for both the laws appears to be faster than available experimental data. Although grain rotation tendency remained similar, the disorientation angles between the predictions of the Voce law and the DD law increase with increasing deformation.
2. Even with similar predictions of the average von Mises stresses for the RVE, spatial distributions of the effective stresses depend on the choice of the hardening law. This difference in the spatial variation of stress distribution increases with the increasing deformation. Specifically, for approximately uniform microstructure, grains with the Taylor factor less than 2.5 show larger stress differences between the two laws.
3. It is difficult to estimate dislocation density distributions on individual slip systems from the Voce law. Instead, only total dislocation densities can be estimated. Further, the DD law results in more localized distribution of the dislocation density than the predictions of the Voce law.
4. With the power law formulation of a constitutive model, dislocation density based hardening law which considers isotropic latent hardening and the dynamic recovery which follows first order of kinetics (i.e. rate of recovery with respect to the shear rate is linearly dependent on the dislocations present on the slip system), predicts higher dislocation density of the grains near the ⟨001⟩ orientations compared to other orientations. Hence, further experimental and simulation analysis of these grains should be carried out.

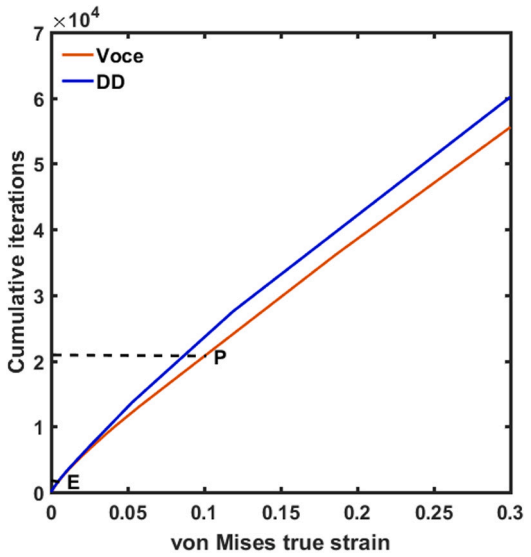

Fig. B.1. Cumulative number of global iterations required for the convergence criterion of the simulations (Eq. (B.6)) as a function of the von Mises true strain. Both the laws show almost a linear behavior during the plastic deformation. For any constant deformation level, the DD hardening required more iterations than the Voce hardening.

CRediT authorship contribution statement

Chaitali S. Patil: Conceptualization, Methodology, Software, Validation, Formal analysis, Investigation, Data curation, Writing – original draft, Writing – review & editing, Visualization. **Supriyo Chakraborty:** Conceptualization, Methodology, Investigation, Writing – review & editing, Visualization. **Stephen R. Niezgoda:** Conceptualization, Methodology, Resources, Supervision, Writing – review & editing, Project administration, Funding acquisition.

Declaration of competing interest

The authors declare that they have no known competing financial interests or personal relationships that could have appeared to influence the work reported in this paper.

Acknowledgments

The authors want to acknowledge the National Science Foundation, Division of Civil, Mechanical and Manufacturing Innovation for their support under the Grant No. CMMI-1662646. SC and CSP want to acknowledge the Simulation Innovation and Modeling Center, The Ohio State University and Ohio Supercomputer Center for providing computational resources. The authors acknowledge thoughtful reviews from anonymous reviewers for improving the manuscript.

Appendix A. Texture update

Rate of the lattice rotation due to the shear accumulation on an individual slip system (plastic spin), $\dot{\omega}_p$, is given by,

$$\dot{\omega}^p(x) = \sum_{s=1}^{N} q^s(x)\dot{\gamma}^s(x) \tag{A.1}$$

where, q^s represents the antisymmetric part of the Schmid tensor. Further, the rate of the lattice rotation at each local point, $\dot{\omega}^*$ is given by Kocks et al. (2000),

$$\dot{\omega}^*(x) = \dot{\omega}(x) - \dot{\omega}_p(x) \tag{A.2}$$

where $\dot{\omega}_p$ is defined in Eq. (A.1), while, $\dot{\omega}$ is the rotation rate of the sample coordinate system which is evaluated as,

$$\dot{\omega}(x) = \frac{1}{2}(\nabla v(x) - \nabla v^T(x)) \tag{A.3}$$

where, $\nabla v(x)$ represents the velocity gradient at the material point x. If the external boundary conditions result in the rigid body rotation of the material, additional spin due to the rigid body rotation should also be considered while evaluating $\dot{\omega}$. Once convergence is achieved, we updated crystal orientations at each material point by the explicit integration of the local rotation rate as defined in the Eq. (A.2).

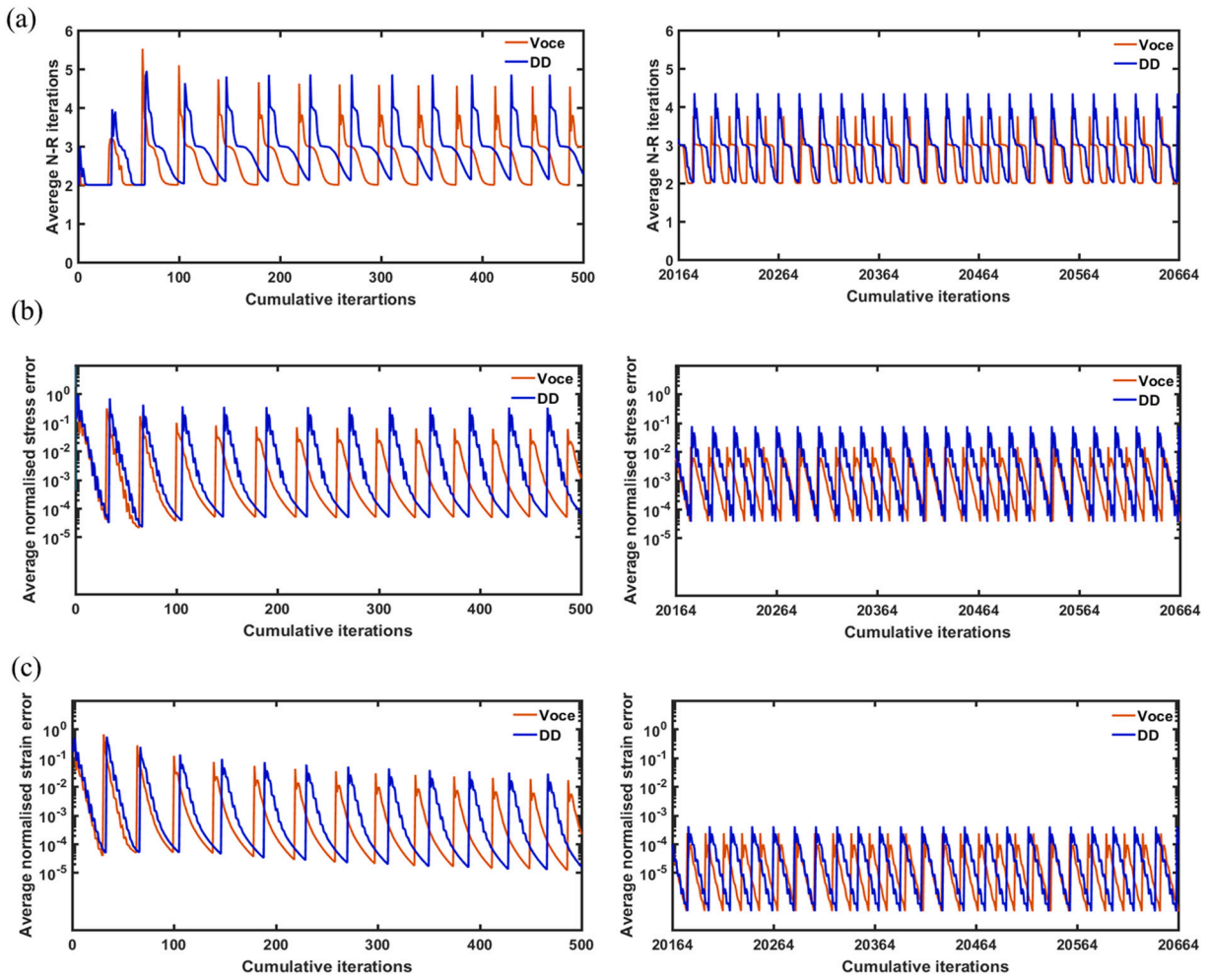

Fig. B.2. (a) Average number of N–R iterations, (b) normalized average stress error and (c) normalized average strain error as a function of the cumulative number of global iterations of the EVP-FFT model for the Voce and the DD hardening laws. Average stress error is normalized by the mean von Mises true stress of the RVE and Average strain error is normalized by the mean von Mises true strain of the RVE. First column in each subfigure, presents the iterations during early stages of the deformation while the last column presents the iterations during the plastic deformation. These two strain levels are marked in Fig. B.1 by the letters 'E' and 'P', respectively. As the DD law requires a larger number of iterations to reach the same strain increment, the effective strain for the Voce law is higher than the DD law at any constant iteration.

Appendix B. Convergence analysis

In the crystal plasticity model, the constitutive relation in Eq. (3) is in the form of rate equation. Hence, the kinematic quantities at each time step are calculated by numerical time integration methods. In this work, we employed the augmented Lagrangian approach with backward Euler method for numerical integration. Michel et al. (2000) proposed the augmented Lagrangian approach based on the implicit time integration method to solve the problems involving large contrast in the local mechanical properties. This scheme was then adopted by Lebensohn et al. (2012) for the polycrystalline material deformation.

In the augmented Lagrangian approach, two stress fields and two strain fields are adjusted iteratively. Here, one of the stress field (λ) satisfies the stress equilibrium and one of the strain field (e) satisfies the strain compatibility. The remaining two fields, auxiliary stress (σ) and strain (ϵ), are related to each other by a constitutive law. Convergence is achieved for new iteration (i+1) when,

$$\frac{\|e_{mn}^{i+1} - \epsilon_{mn}^{i+1}\|}{\langle e_{vM} \rangle} < \delta \quad \text{and} \quad \frac{\|\lambda_{mn}^{i+1} - \sigma_{mn}^{i+1}\|}{\langle \sigma_{vM} \rangle} < \delta \tag{B.6}$$

Here, $\langle e_{vM} \rangle$ and $\langle \sigma_{vM} \rangle$ represent the average von Mises true strain and true stress, respectively. In this study, we used error tolerance (δ) equal to 5×10^{-5}. Fig. B.1 presents the cumulative number of global iterations (i) required to satisfy the convergence criterion (Eq. (B.6)) for both the hardening rules as a function of the equivalent true strain. At any strain, cumulative iterations required for

the DD law are higher than the Voce law. Specifically, for each strain increment of 1×10^{-4}, the DD law required an average of 26, 21 and 19 iterations for the stain ranges of 0–0.05, 0.05–0.1 and 0.1–0.3, respectively. In the same strain ranges, the Voce law required an average of 23, 18 and 17 iterations at each strain increment. It can be also noted that the solution requires slightly more number iterations at smaller strains than at the larger strains for both the laws.

Moreover, augmented Lagrangian scheme involves nullification of the residual (R) at each material point (x). This residual R defined, using Einstein summation notation, as Lebensohn et al. (2012),

$$R_{kl}(\sigma_{kl}^{i+1}) = \sigma_{kl}^{i+1} + C_{klmn}^{0} e_{mn}^{i+1} - \lambda_{kl}^{i} - C_{klmn}^{0} e_{mn}^{i+1} \tag{B.7}$$

This non-linear equation is solved by using the Modified Newton–Raphson (N–R) algorithm. Thus, solver iterates through the internal N–R loops for a single global iteration (i). Hence, in Fig. B.2, we present the convergence analysis for N–R iterations near two different strain levels —(1) Initial stages of the deformation involving elastic to plastic transition. The strain level is marked by a letter 'E' in Fig. B.1. (2) Later stage of the plastic deformation which is marked by a letter 'P' in Fig. B.1. Fig. B.2(a) shows the average number of N–R iterations required for the nullification of residual R (Eq. (B.7)) as a function of cumulative numbers of global iterations. As the DD hardening requires larger number of iterations to reach the same strain increment, the effective strain for the Voce law is higher than the DD law at any constant iteration (i) considered in Fig. B.2. For both the hardening laws, average numbers of N–R steps decrease as the global convergence for the outer loop (Eq. (B.6)) is approached. Maximum numbers of N–R iterations required for the solution are less than 6 for both of the considered intervals of global iterations. This trend is consistent with the observation of Lebensohn et al. (2012). These authors showed that approximately 2 to 8 average N–R iterations were required during early stages of the deformation with significant hardening of the slip systems and error threshold (δ) of 10^{-5}. Except for the very early stages of the deformation, the Voce hardening required smaller number of N–R iterations than the DD law. To understand a quantitative implication of this difference, consider the difference between the average N–R steps at beginning of any deformation step. This difference is approximately 0.2 in the early stage of the deformation, while, it increased to 0.5 in the plastic regime. Hence, the DD law required at least 1.05×10^{6} more calculations for each global iteration during plastic regime, as the RVE is of the size $128 \times 128 \times 128$. Thus, the Voce hardening is computationally more efficient than the DD law. Fig. B.2(b) also reports the average difference between the $\sigma(x)$ and $\lambda(x)$, normalized by the mean von Mises true stress of the RVE, as a function of the cumulative iterations. Similarly, the normalized strain error is shown in Fig. B.2(c). The maximum stress errors during the each global iteration is higher for the DD law than the Voce law; while the strain errors are approximately equal. Fig. B.2 also illustrates that normalized stress and strain errors are higher for the initial stages of the deformation than the later stages of the deformation.

Appendix C. Supplementary data

Supplementary material related to this article can be found online at https://doi.org/10.1016/j.ijplas.2021.103099.

References

Abdolvand, H., Wright, J.P., Wilkinson, A.J., 2018. On the state of deformation in a polycrystalline material in three-dimension: elastic strains, lattice rotations, and deformation mechanisms. Int. J. Plast. 106, 145–163. http://dx.doi.org/10.1016/j.ijplas.2018.03.006.

Adam, K., Zöllner, D., Field, D.P., 2018. 3D microstructural evolution of primary recrystallization and grain growth in cold rolled single-phase aluminum alloys. Modelling Simulation Mater. Sci. Eng. 26, 035011. http://dx.doi.org/10.1088/1361-651X/aaa146.

Alankar, A., Field, D.P., Zbib, H.M., 2012. Explicit incorporation of cross-slip in a dislocation density-based crystal plasticity model. Phil. Mag. 92, 3084–3100. http://dx.doi.org/10.1080/14786435.2012.685964.

Albiez, J., Erdle, H., Weygand, D., Böhlke, T., 2019. A gradient plasticity creep model accounting for slip transfer/activation at interfaces evaluated for the intermetallic NiAl-9Mo. Int. J. Plast. 113, 291–311. http://dx.doi.org/10.1016/j.ijplas.2018.10.006.

Asaro, R.J., Needleman, A., 1985. Overview (42) texture development and strain hardening in rate dependent polycrystals. Acta Metall. 33, 923–953. http://dx.doi.org/10.1016/0001-6160(85)90188-9.

Bachmann, F., Hielscher, R., Schaeben, H., 2010. Texture analysis with MTEX–free and open source software toolbox. In: Solid State Phenomena. Trans Tech Publ., pp. 63–68. http://dx.doi.org/10.4028/www.scientific.net/SSP.160.63.

Bailey, J., 1963. The dislocation density, flow stress and stored energy in deformed polycrystalline copper. Phil. Mag. 8, 223–236. http://dx.doi.org/10.1080/14786436308211120.

Baudoin, P., Hama, T., Takuda, H., 2019. Influence of critical resolved shear stress ratios on the response of a commercially pure titanium oligocrystal: crystal plasticity simulations and experiment. Int. J. Plast. 115, 111–131. http://dx.doi.org/10.1016/j.ijplas.2018.11.013.

Berbenni, S., Taupin, V., Lebensohn, R.A., 2020. A fast fourier transform-based mesoscale field dislocation mechanics study of grain size effects and reversible plasticity in polycrystals. J. Mech. Phys. Solids 135, 103808. http://dx.doi.org/10.1016/j.jmps.2019.103808.

Bonneville, J., Escaig, B., Martin, J., 1988. A study of cross-slip activation parameters in pure copper. Acta Metall. 36, 1989–2002. http://dx.doi.org/10.1016/0001-6160(88)90301-X.

Bronkhorst, C., Kalidindi, S., Anand, L., 1992. Polycrystalline plasticity and the evolution of crystallographic texture in FCC metals. Phil. Trans. R. Soc. A 341, 443–477. http://dx.doi.org/10.1098/rsta.1992.0111.

Buchheit, T.E., Wellman, G.W., Battaile, C.C., 2005. Investigating the limits of polycrystal plasticity modeling. Int. J. Plast. 21, 221–249. http://dx.doi.org/10.1016/j.ijplas.2003.10.009.

Bunge, H.J., 2013. Texture Analysis in Materials Science: Mathematical Methods. Elsevier.

Capolungo, L., 2011. Dislocation junction formation and strength in magnesium. Acta Mater. 59, 2909–2917. http://dx.doi.org/10.1016/j.actamat.2011.01.026.

Chen, L., Chen, J., Lebensohn, R., Ji, Y., Heo, T., Bhattacharyya, S., Chang, K., Mathaudhu, S., Liu, Z., Chen, L.Q., 2015. An integrated fast Fourier transform-based phase-field and crystal plasticity approach to model recrystallization of three dimensional polycrystals. Comput. Methods Appl. Mech. Engrg. 285, 829–848. http://dx.doi.org/10.1016/j.cma.2014.12.007.

Cruzado, A., Lucarini, S., LLorca, J., Segurado, J., 2018. Crystal plasticity simulation of the effect of grain size on the fatigue behavior of polycrystalline Inconel 718. Int. J. Fatigue 113, 236–245. http://dx.doi.org/10.1016/j.ijfatigue.2018.04.018.

Demir, E., Gutierrez-Urrutia, I., 2020. Investigation of strain hardening near grain boundaries of an aluminum oligocrystal: Experiments and crystal based finite element method. Int. J. Plast. 102898. http://dx.doi.org/10.1016/j.ijplas.2020.102898.

Eghtesad, A., Knezevic, M., 2020. A full-field crystal plasticity model including the effects of precipitates: Application to monotonic, load reversal, and low-cycle fatigue behavior of Inconel 718. Mater. Sci. Eng. A 140478. http://dx.doi.org/10.1016/j.msea.2020.140478.

Esteban-Manzanares, G., Santos-Güemes, R., Papadimitriou, I., Martínez, E., LLorca, J., 2020. Influence of the stress state on the cross-slip free energy barrier in Al: An atomistic investigation. Acta Mater. 184, 109–119. http://dx.doi.org/10.1016/j.actamat.2019.10.055.

Estrin, Y., Mecking, H., 1984. A unified phenomenological description of work hardening and creep based on one-parameter models. Acta Metall. 32, 57–70. http://dx.doi.org/10.1016/0001-6160(84)90202-5.

Franciosi, P., 1985. The concepts of latent hardening and strain hardening in metallic single crystals. Acta Metall. 33, 1601–1612. http://dx.doi.org/10.1016/0001-6160(85)90154-3.

Githens, A., Ganesan, S., Chen, Z., Allison, J., Sundararaghavan, V., Daly, S., 2020. Characterizing microscale deformation mechanisms and macroscopic tensile properties of a high strength magnesium rare-earth alloy: A combined experimental and crystal plasticity approach. Acta Mater. 186, 77–94. http://dx.doi.org/10.1016/j.actamat.2019.12.012.

Groeber, M.A., Jackson, M.A., 2014. DREAM.3D: A digital representation environment for the analysis of microstructure in 3D. Integr. Mater. Manuf. Innov. 3, 5. http://dx.doi.org/10.1186/2193-9772-3-5.

Guan, Y., Chen, B., Zou, J., Britton, T.B., Jiang, J., Dunne, F.P., 2017. Crystal plasticity modelling and HR-DIC measurement of slip activation and strain localization in single and oligo-crystal Ni alloys under fatigue. Int. J. Plast. 88, 70–88. http://dx.doi.org/10.1016/j.ijplas.2016.10.001.

Guery, A., Hild, F., Latourte, F., Roux, S., 2016. Slip activities in polycrystals determined by coupling dic measurements with crystal plasticity calculations. Int. J. Plast. 81, 249–266. http://dx.doi.org/10.1016/j.ijplas.2016.01.008.

Gustafson, S., Ludwig, W., Shade, P., Naragani, D., Pagan, D., Cook, P., Yildirim, C., Detlefs, C., Sangid, M.D., 2020. Quantifying microscale drivers for fatigue failure via coupled synchrotron X-ray characterization and simulations. Nature Commun. 11, 1–10. http://dx.doi.org/10.1038/s41467-020-16894-2.

Haouala, S., Lucarini, S., LLorca, J., Segurado, J., 2020. Simulation of the Hall-Petch effect in FCC polycrystals by means of strain gradient crystal plasticity and FFT homogenization. J. Mech. Phys. Solids 134, 103755. http://dx.doi.org/10.1016/j.jmps.2019.103755.

Huang, X., 1998. Grain orientation effect on microstructure in tensile strained copper. Scr. Mater. 38, http://dx.doi.org/10.1016/S1359-6462(98)00051-7.

Hutchinson, J.W., 1976. Bounds and self-consistent estimates for creep of polycrystalline materials. Proc. R. Soc. Lond. Ser. A Math. Phys. Eng. Sci. 348, 101–127. http://dx.doi.org/10.1098/rspa.1976.0027.

Jackson, P., 1983. The role of cross-slip in the plastic deformation of crystals. Mater. Sci. Eng. 57, 39–47. http://dx.doi.org/10.1016/0025-5416(83)90025-3.

Jackson, P., Basinski, Z., 1967. Latent hardening and the flow stress in copper single crystals. Can. J. Phys. 45, 707–735. http://dx.doi.org/10.1139/p67-055.

Jiang, J., Britton, T.B., Wilkinson, A.J., 2015. The orientation and strain dependence of dislocation structure evolution in monotonically deformed polycrystalline copper. Int. J. Plast. 69, 102–117. http://dx.doi.org/10.1016/j.ijplas.2015.02.005.

Kanjarla, A., Lebensohn, R., Balogh, L., Tomé, C., 2012. Study of internal lattice strain distributions in stainless steel using a full-field elasto-viscoplastic formulation based on fast Fourier transforms. Acta Mater. 60, 3094–3106. http://dx.doi.org/10.1016/j.actamat.2012.02.014.

Kim, D.K., Woo, W., Park, W.W., Im, Y.T., Rollett, A., 2017. Mesoscopic coupled modeling of texture formation during recrystallization considering stored energy decomposition. Comput. Mater. Sci. 129, 55–65. http://dx.doi.org/10.1016/j.commatsci.2016.11.048.

Kocks, U.F., Tomé, C.N., Wenk, H.R., 2000. Texture and anisotropy: preferred orientations in polycrystals and their effect on materials properties. Cambridge University Press.

Kotha, S., Ozturk, D., Ghosh, S., 2020. Uncertainty-quantified parametrically homogenized constitutive models (UQ-PHCMs) for dual-phase α/β titanium alloys. Npj Comput. Mater. 6, 1–20. http://dx.doi.org/10.1038/s41524-020-00379-3.

Kubin, L., Hoc, T., Devincre, B., 2009. Dynamic recovery and its orientation dependence in face-centered cubic crystals. Acta Mater. 57, 2567–2575. http://dx.doi.org/10.1016/j.actamat.2009.02.013.

Kuykendall, W.P., Wang, Y., Cai, W., 2020. Stress effects on the energy barrier and mechanisms of cross-slip in FCC nickel. J. Mech. Phys. Solids 144, 104105. http://dx.doi.org/10.1016/j.jmps.2020.104105.

Lebensohn, R.A., Kanjarla, A.K., Eisenlohr, P., 2012. An elasto-viscoplastic formulation based on fast fourier transforms for the prediction of micromechanical fields in polycrystalline materials. Int. J. Plast. 32, 59–69. http://dx.doi.org/10.1016/j.ijplas.2011.12.005.

Lebensohn, R.A., Rollett, A.D., 2020. Spectral methods for full-field micromechanical modelling of polycrystalline materials. Comput. Mater. Sci. 173, 109336. http://dx.doi.org/10.1016/j.commatsci.2019.109336.

Lee, M., Lim, H., Adams, B., Hirth, J., Wagoner, R., 2010. A dislocation density-based single crystal constitutive equation. Int. J. Plast. 26, 925–938. http://dx.doi.org/10.1016/j.ijplas.2009.11.004.

Lim, H., Battaile, C.C., Bishop, J.E., Foulk III, J.W., 2019. Investigating mesh sensitivity and polycrystalline RVEs in crystal plasticity finite element simulations. Int. J. Plast. 121, 101–115. http://dx.doi.org/10.1016/j.ijplas.2019.06.001.

Lim, H., Carroll, J., Battaile, C.C., Buchheit, T., Boyce, B., Weinberger, C., 2014. Grain-scale experimental validation of crystal plasticity finite element simulations of tantalum oligocrystals. Int. J. Plast. 60, 1–18. http://dx.doi.org/10.1016/j.ijplas.2014.05.004.

Linne, M.A., Bieler, T.R., Daly, S., 2020. The effect of microstructure on the relationship between grain boundary sliding and slip transmission in high purity aluminum. Int. J. Plast. 135, 102818. http://dx.doi.org/10.1016/j.ijplas.2020.102818.

Ma, A., Roters, F., 2004. A constitutive model for fcc single crystals based on dislocation densities and its application to uniaxial compression of aluminium single crystals. Acta Mater. 52, 3603–3612. http://dx.doi.org/10.1016/j.actamat.2004.04.012.

Madec, R., Devincre, B., Kubin, L.P., 2002. From dislocation junctions to forest hardening. Phys. Rev. Lett. 89, 255508. http://dx.doi.org/10.1103/PhysRevLett.89.255508.

Madec, R., Kubin, L.P., 2017. Dislocation strengthening in FCC metals and in BCC metals at high temperatures. Acta Mater. 126, 166–173. http://dx.doi.org/10.1016/j.actamat.2016.12.040.

Magri, M., Lucarini, S., Lemoine, G., Adam, L., Segurado, J., 2021. An fft framework for simulating non-local ductile failure in heterogeneous materials. Comput. Methods Appl. Mech. Engrg. 380, 113759. http://dx.doi.org/10.1016/j.cma.2021.113759.

Malka-Markovitz, A., Devincre, B., Mordehai, D., 2021. A molecular dynamics-informed probabilistic cross-slip model in discrete dislocation dynamics. Scr. Mater. 190, 7–11. http://dx.doi.org/10.1016/j.scriptamat.2020.08.008.

Mangal, A., Holm, E.A., 2018. Applied machine learning to predict stress hotspots I: Face centered cubic materials. Int. J. Plast. 111, 122–134. http://dx.doi.org/10.1016/j.ijplas.2018.07.013.

Marano, A., Gélébart, L., Forest, S., 2021. FFT-Based simulations of slip and kink bands formation in 3D polycrystals: influence of strain gradient crystal plasticity. J. Mech. Phys. Solids 149, 104295. http://dx.doi.org/10.1016/j.jmps.2021.104295.

Mecking, H., Kocks, U., 1981. Kinetics of flow and strain-hardening. Acta Metall. 29, 1865–1875. http://dx.doi.org/10.1016/0001-6160(81)90112-7.

Michel, J., Moulinec, H., Suquet, P., 2000. A computational method based on augmented Lagrangians and fast Fourier transforms for composites with high contrast. CMES (Comput. Model. Eng. Sci.) 1, 79–88. http://dx.doi.org/10.3970/cmes.2000.001.239.

Moulinec, H., Suquet, P., 1994. A fast numerical method for computing the linear and nonlinear mechanical properties of composites. C. R. Acad. Sci., Paris II.

Moulinec, H., Suquet, P., 1998. A numerical method for computing the overall response of nonlinear composites with complex microstructure. Comput. Methods Appl. Mech. Engrg. 157, 69–94. http://dx.doi.org/10.1016/S0045-7825(97)00218-1.

Mughrabi, H., Ungar, T., Kienle, W., Wilkens, M., 1986. Long-range internal stresses and asymmetric X-ray line-broadening in tensile-deformed [001]-orientated copper single crystals. Phil. Mag. A 53, 793–813. http://dx.doi.org/10.1080/01418618608245293.

Naaman, H., Talreja, R., Jensen, D.J., Hansen, N., 1987. Development of deformation textures in polycrystalline copper experiments and model predictions. Textures Microstruct. 7, 149–170.

Nagra, J.S., Brahme, A., Lévesque, J., Mishra, R., Lebensohn, R.A., Inal, K., 2020. A new micromechanics based full field numerical framework to simulate the effects of dynamic recrystallization on the formability of HCP metals. Int. J. Plast. 125, 210–234. http://dx.doi.org/10.1016/j.ijplas.2019.09.011.

Naragani, D., Sangid, M.D., Shade, P.A., Schuren, J.C., Sharma, H., Park, J.S., Kenesei, P., Bernier, J.V., Turner, T.J., Parr, I., 2017. Investigation of fatigue crack initiation from a non-metallic inclusion via high energy X-ray diffraction microscopy. Acta Mater. 137, 71–84. http://dx.doi.org/10.1016/j.actamat.2017.07.027.

Panchal, J.H., Kalidindi, S.R., McDowell, D.L., 2013. Key computational modeling issues in integrated computational materials engineering. Comput. Aided Des. 45, 4–25. http://dx.doi.org/10.1016/j.cad.2012.06.006.

Paramatmuni, C., Kanjarla, A.K., 2019. A crystal plasticity FFT based study of deformation twinning, anisotropy and micromechanics in HCP materials: Application to AZ31 alloy. Int. J. Plast. 113, 269–290. http://dx.doi.org/10.1016/j.ijplas.2018.10.007.

Pinna, C., Lan, Y., Kiu, M., Efthymiadis, P., Lopez-Pedrosa, M., Farrugia, D., 2015. Assessment of crystal plasticity finite element simulations of the hot deformation of metals from local strain and orientation measurements. Int. J. Plast. 73, 24–38. http://dx.doi.org/10.1016/j.ijplas.2015.05.015.

Pokharel, R., Lind, J., Kanjarla, A.K., Lebensohn, R.A., Li, S.F., Kenesei, P., Suter, R.M., Rollett, A.D., 2014. Polycrystal plasticity: comparison between grain-scale observations of deformation and simulations. Annu. Rev. Condens. Matter Phys. 5, 317–346. http://dx.doi.org/10.1146/annurev-conmatphys-031113-133846.

Rehrl, C., Völker, B., Kleber, S., Antretter, T., Pippan, R., 2012. Crystal orientation changes: A comparison between a crystal plasticity finite element study and experimental results. Acta Mater. 60, 2379–2386. http://dx.doi.org/10.1016/j.actamat.2011.12.052.

Ricciardi, D.E., Chkrebtii, O.A., Niezgoda, S.R., 2020. Uncertainty quantification accounting for model discrepancy within a random effects bayesian framework. Integr. Mater. Manuf. Innov. 9, 181–198. http://dx.doi.org/10.1007/s40192-020-00176-2.

Roters, F., Diehl, M., Shanthraj, P., Eisenlohr, P., Reuber, C., Wong, S.L., Maiti, T., Ebrahimi, A., Hochrainer, T., Fabritius, H.O., et al., 2019. DAMASK–the Düsseldorf Advanced Material Simulation Kit for modeling multi-physics crystal plasticity, thermal, and damage phenomena from the single crystal up to the component scale. Comput. Mater. Sci. 158, 420–478. http://dx.doi.org/10.1016/j.commatsci.2018.04.030.

Roters, F., Eisenlohr, P., Hantcherli, L., Tjahjanto, D.D., Bieler, T.R., Raabe, D., 2010. Overview of constitutive laws, kinematics, homogenization and multiscale methods in crystal plasticity finite-element modeling: Theory, experiments, applications. Acta Mater. 58, 1152–1211. http://dx.doi.org/10.1016/j.actamat.2009.10.058.

Sam, D.D., Adams, B.L., 1986. Orientation and strain dependence of stored energy of cold work in axisymmetric copper. Metall. Trans. A 17, 513–517. http://dx.doi.org/10.1007/BF02643958.

Sedaghat, O., Abdolvand, H., 2021. A non-local crystal plasticity constitutive model for hexagonal close-packed polycrystals. Int. J. Plast. 136, 102883. http://dx.doi.org/10.1016/j.ijplas.2020.102883.

Shen, Y.F., Liu, H., Suter, R.M., 2020. Voxel-based strain tensors from near-field High Energy Diffraction Microscopy. Curr. Opin. Solid State Mater. Sci. 24, 100852. http://dx.doi.org/10.1016/j.cossms.2020.100852.

Sills, R.B., Bertin, N., Aghaei, A., Cai, W., 2018. Dislocation networks and the microstructural origin of strain hardening. Phys. Rev. Lett. 121, 085501. http://dx.doi.org/10.1103/PhysRevLett.121.085501.

Slone, C., Chakraborty, S., Miao, J., George, E.P., Mills, M.J., Niezgoda, S., 2018. Influence of deformation induced nanoscale twinning and FCC-HCP transformation on hardening and texture development in medium-entropy CrCoNi alloy. Acta Mater. 158, 38–52. http://dx.doi.org/10.1016/j.actamat.2018.07.028.

Stout, M., O'Rourke, J., 1989. Experimental deformation textures of OFE copper and 70: 30 brass from wire drawing, compression, and torsion. Metall. Trans. A 20, 125–131. http://dx.doi.org/10.1007/BF02647499.

Takeuchi, T., 1975. Work hardening of copper single crystals with multiple glide orientations. Trans. Japan Inst. Met. 16, 629–640. http://dx.doi.org/10.2320/matertrans1960.16.629.

Taylor, G.I., 1934. The mechanism of plastic deformation of crystals. Part I.—Theoretical. Proc. R. Soc. A 145, 362–387. http://dx.doi.org/10.1098/rspa.1934.0106.

Tome, C., Canova, G., Kocks, U., Christodoulou, N., Jonas, J., 1984. The relation between macroscopic and microscopic strain hardening in FCC polycrystals. Acta Metall. 32, 1637–1653. http://dx.doi.org/10.1016/0001-6160(84)90222-0.

Tomé, C., Lebensohn, R., 2007. Visco-plastic self-consistent (vpsc). 6, Los Alamos National Laboratory (USA) and Universidad Nacional de Rosario (Argentina).

Vorbrugg, W., Goetting, H.C., Schwink, C., 1971. Work-hardening and surface investigations on copper single crystals oriented for multiple glide. Phys. Status Solidi b 46, 257–264. http://dx.doi.org/10.1002/pssb.2220460123.

Wan, V., MacLachlan, D., Dunne, F., 2014. A stored energy criterion for fatigue crack nucleation in polycrystals. Int. J. Fatigue 68, 90–102. http://dx.doi.org/10.1016/j.ijfatigue.2014.06.001.

Wulfinghoff, S., Böhlke, T., 2015. Gradient crystal plasticity including dislocation-based work-hardening and dislocation transport. Int. J. Plast. 69, 152–169. http://dx.doi.org/10.1016/j.ijplas.2014.12.003.

Zhang, Z., Lunt, D., Abdolvand, H., Wilkinson, A.J., Preuss, M., Dunne, F.P., 2018. Quantitative investigation of micro slip and localization in polycrystalline materials under uniaxial tension. Int. J. Plast. 108, 88–106. http://dx.doi.org/10.1016/j.ijplas.2018.04.014.

Zhao, P., Low, T.S.E., Wang, Y., Niezgoda, S.R., 2016. An integrated full-field model of concurrent plastic deformation and microstructure evolution: Application to 3D simulation of dynamic recrystallization in polycrystalline copper. Int. J. Plast. 80, 38–55. http://dx.doi.org/10.1016/j.ijplas.2015.12.010.